Giant Switchable Photovoltaic Effect in Organometal Trihalide Perovskite Devices

Zhengguo Xiao[1,2†], Yongbo Yuan[1,2†], Yuchuan Shao [1,2†], Qi Wang,[1,2] Qingfeng Dong,[1,2] Cheng Bi[1,2], Pankaj Sharma[2,3], Alexei Gruverman[2,3] and Jinsong Huang[1,2] *

[1]Department of Mechanical and Materials Engineering, University of Nebraska-Lincoln, Lincoln, Nebraska 68588-0656, USA. [2]Nebraska Center for Materials, Nanoscience, University of Nebraska-Lincoln, Lincoln, Nebraska 68588-0298, USA. [3]Department of Physics and Astronomy, University of Nebraska-Lincoln, Lincoln, Nebraska 68588-0299, USA

*Correspond to: jhuang2@unl.edu

Organolead trihalide perovskite (OTP) materials are emerging as naturally abundant materials for low-cost, solution processed and highly efficient solar cells[1-9]. Here we show that, in OTP-based photovoltaic devices with vertical and lateral cell configuration, the photocurrent direction can be switched repeatedly by applying a small electric field of <1 V/μm. The switchable photocurrent, generally observed in devices based on ferroelectric materials, reached 20.1 mA/cm^2 under one sun illumination in OTP devices with vertical architecture, which is four orders of magnitude larger than that measured in other ferroelectric photovoltaic devices[10,11]. This field-switchable photovoltaic effect can be explained by the formation of reversible *p-i-n* structures induced by ion drift in the perovskite layer. The demonstration of switchable OTP photovoltaics and electric-field manipulated doping paves the way for innovative solar cell designs and for the exploitation of OTP materials in electrically- and optically- readable memristors and circuits.

The vertical structure device has a layered structure of indium tin oxide (ITO)/poly(3,4-ethylenedioxythiophene):poly(4-styrenesulfonate) (PEDOT:PSS)/Perovskite/Au as shown in Fig. 1a, where the methylammonium lead iodide ($MAPbI_3$) perovskite layer was formed by the interdiffusion of lead iodine (PbI_2) and methylammonium halide (MAI) stacking layers[12]. The

as-prepared devices with 300 nm thick perovskite films have a J_{SC} of 8.5 mA/cm^2 and V_{OC} of 0.18 V (Fig. S1), despite that the work function of PEDOT:PSS and Au electrodes are almost the same. This might be due to the different interfacial electronic structures at the perovskite/PEDOT:PSS and perovskite/Au contacts. A large memristive effect from these devices was identified both in the dark and under illumination, which showed a scanning history dependent current output (Fig. S2). The diode direction can be switched during the scanning process in the dark as shown in Fig. 1b. The on/off ratio of the dark current is >10^3 and >10^2 at a bias of -1.0 V and 0.7 V, respectively. The devices can also be poled by a constant bias pulse with a duration of 5~30 s (Fig. S3a-b). The device with a perovskite layer thickness of 1,015 nm was switched by a small bias of 1.0 V (Fig. S3c), which corresponds to a minimal poling electric field of < 1 V/μm.

The switchable diode in the dark resulted in a giant switchable photovoltaic effect under illumination. In contrast to the switchable photovoltaics using bismuth ferrite materials with J_{SC} typically on the order of ~μA/cm^2 [10,11], the J_{SC} of the OTP devices was switched between 18.6 and -20.1 mA/cm^2 (Fig. 1c) under one sun illumination, which is comparable to that of the optimized perovskite solar cells[1-5,13]. This indicates that most of the photogenerated excitons dissociated to free charges in the perovskite layer even without an electron or hole accepting layer, and the free charges were efficiently collected by the electrodes regardless of the diode directions. The photocurrents showed varied hysteresis loops with changed scanning rates, while the J_{SC} remained almost unchanged and the V_{OC} was around 0.15 V lower at a lower scanning rate of 0.25 V/s, as shown in Fig. S2b-d. The photocurrent direction after poling remained unchanged after storing the device for two months under ambient illumination in the glove box (Fig. S4). The V_{OC} was switched between 0.42 V and -0.73 V. There is a variation in J_{SC} and V_{OC}

from different devices; and some of them showed a larger V_{OC} close to 0.9 V but a relatively smaller J_{SC} of 8 mA/cm^2 (Fig. S5). The average V_{OC} and J_{SC} of the vertical structure devices were ±0.65 V and ±18.5 mA/cm^2, respectively (Fig. S5). A positive poling (electric field pointing from PEDOT:PSS to Au) resulted in a positive V_{OC}. A typical device was switched more than 750 times with the V_{OC} in the first 10 and last 10 poling circles shown in Fig. 1d. The photocurrent direction of the device can survive after 750 poling circles. After positive poling, the V_{OC} remained almost constant at 0.42 V, while the V_{OC} after negative poling showed switching fatigue from 0.73 V to 0.21 V. The switchable photovoltaic phenomenon was universally demonstrated using other organolead trihalide perovskite materials, such as $CH_3NH_3PbI_{3-x}Cl_x$, $HC(NH_2)_2PbI_3$ and $CH_3NH_3PbBr_3$ (Fig. S6), and with many other top electrodes including nickel, gallium and platinum (Fig. S7), but not Al or Ag, due to the severe chemical reaction of perovskite with Al and Ag.

We continued to demonstrate the switchable photovoltaic effect in lateral structure devices because of the very low electric field of 1 V/μm needed for poling and the absence of electrode selectivity shown in the vertical structure devices. Fig. 2a schematically shows that the photovoltaic device has a lateral symmetric structure of Au/OTP/Au/OTP/…, where tens to hundreds of cells are connected in series. Fig. 2b shows the optical image of a Au electrode pattern fabricated by photolithography, where electrode spacing is 8 μm. As shown in Fig. 2c, the non-poled device had no photovoltaic effect with zero V_{OC} because of the symmetrical electrodes, while the poled single cell showed a V_{OC} of 0.48 V under 0.25 sun illumination after poling at 10 V for ~100 s. The photovoltaic direction after poling was consistent with that of vertical structure devices. The photovoltaic direction was flipped by a reversed poling bias. In contrast to ferroelectric photovoltaics[14], the V_{OC} of a single device after poling remains almost

constant at around 0.50 V regardless of the electrode spacing variation from 8 to 100 μm (Fig. S9). The J_{SC} of the device with 8 μm electrode spacing is 0.1 mA/cm^2. The smaller J_{SC} in the lateral structure devices is due to the much larger electrode spacing than the charge diffusion length in perovskite materials[15,16]. The statistics of the performance of the lateral structure devices was shown in Fig. S8. The largest absolute V_{OC} and J_{SC} value reached 0.88 V and 0.11 mA/cm^2, and the average V_{OC} and J_{SC} of the lateral structure devices were ±0.50 V and ±0.075 mA/cm^2 respectively. As shown in Fig. 2d, the V_{OC} of lateral photovoltaic devices connected in series is the sum of each unit cell, while the J_{SC} remains almost constant, indicating a uniform performance of each unit cell. A large V_{OC} of 47 V was observed for the devices with 125 unit cells connected in series under illumination of 25 mW/cm^2.

In order to find out the origin of the switchable photovoltaic effect in OTP devices, we examined three possible mechanisms which have been reported for switchable photovoltaic or memristor behavior, which was also speculated to result in photocurrent hysteresis with a changed photocurrent scanning direction and scanning rate in some perovskite photovoltaic devices[17]: 1) ferroelectricity of the photoactive layer[18]; 2) charge traps in the active layer's surface[17,19]; and 3) motion and accumulation of ions induced doping effect[10,20]. Some theoretical calculation predicted strong ferroelectricity of $MAPbI_3$ with a polarization charge density on the order of 38 C/m^2 [21,22]. However, no ferroelectric polarization was detected from these devices with comparable voltage scanning rates as in photovoltaic study when they were measured at both room temperature and 77 K (Fig. S10). PFM imaging and hysteresis loop measurements did not show anything resembling ferroelectric activity in the $MAPbI_3$ perovskite films, i.e. there were weak PFM amplitude and phase signals and no hysteresis switching activity, despite the application of a much higher bias than in the switchable photovoltaic studies. In addition, the

ferroelectric photovoltaic effect can be excluded by the non-changed photovoltage with respect to the electrode spacing in the lateral structure devices, (Fig. S9) and diminished switching behavior at reduced temperature (Fig. S14). Our finding does not rule out ferroelectricity in $MAPbI_3$ in principle as more measurements (such as temperature-dependent dielectric and structural testing) are required to clarify this issue. The charge-trapping mechanism can also be excluded because it cannot explain the flipped photovoltage and photocurrent direction, and the persistent photocurrent output long after poling shown in Fig. S11. It was previously reported that similar halide containing perovskites, such as $CsPbCl_3$ and $CsPbBr_3$, are good halide ion vacancy conductors at elevated temperatures[23]. We ascribe switchable photovoltaic to the ion drift under the electric field in the perovskite layer. Theoretical calculation predicted the $V_{Pb}^{\bullet}$ and $V_{MA}^{\bullet}$ could result in *p*-type doping, while the V_I' result in *n*-type doping in $MAPbI_3$[24,25], which was verified experimentally by us in the study of composition dependent self-doping behavior in $MAPbI_3$[26]. In this scenario, the electric field drives the drift of charged V_I', $V_{Pb}^{\bullet}$ and/or $V_{MA}^{\bullet}$, which have low formation energy in $MAPbI_3$[24,25], to the area near electrode and forms the *p*-*i*-*n* structure. Our scenario for the switchable photovoltaic is illustrated in Fig. 3a-b using vertical structure devices as an example. The positively charged ions or vacancies moved to the Au side during positive poling and accumulated there, which caused *n*-doping in perovskite at the Au side. Similarly, the left negative space charge layer can *p*-dope the perovskite layer close to PEDOT:PSS, which forms a *p*-*i*-*n* homojunction structure. A reversed bias can flip the *p*-*i*-*n* structure to *n*-*i*-*p* by driving the ions or ion vacancies to drift in the opposite direction. The memristive dark- and photo-current hysteresis can also be well explained by the time-dependent drift of ions under the field[27].

To test this scenario, we first measured the doping caused band-bending in perovskite close to the top Au electrode after poling in the vertical structure devices by Kelvin probe force microscopy (KPFM). The *p*- or *n*-doping should induce an increase or reduction of the work function for the perovskite top surface, respectively, as illustrated by the energy diagram in Fig. 3c. The long retention of the diode direction indicates that the poling induced composition change or work function change is stable after poling. Au electrodes could be easily peeled off by a scotch tape, which exposed the poled perovskite films. Fig. 3d illustrated the films used for the KPFM study, where some unpeeled Au areas were intentionally left as work function reference. As shown in Fig. 3 e-f, the work function of the perovskite films was ~0.22 V lower than that of Au after positive poling, and comparable to that of Au after negative poling, which agreed well with the energy diagram in Fig. 3c and thus supports the proposed doping mechanism. The surface topography showed no obvious change in the poling areas (Fig. S12) which excluded the effect of topography to the surface potential measurement. The discrepancy of the perovskite work function change with V_{OC} can be explained by the possible surface contamination by the residues of Au after peeling and/or by moisture/oxygen because the KPFM measurement was conducted in air. Finally, semiconductor doping generally causes photoluminescence (PL) quench, which was also observed for the *p*- and *n*-doped perovskite region close to both Au and PEDOT:PSS sides, as shown in Fig.3 g-h.

Another conclusive evidence for the drift of ions during the poling process comes from the observation of composition and morphology changes during the poling of a lateral structure device. In this study, the device was intentionally poled for a much longer time (2 hours) than was needed for the doping effect so that the change in perovskite composition/morphology was discernable. The transparency of the perovskite film was monitored in situ under an optical

microscopy, as illustrated by the measurement setup in Fig. 4a. The dynamic process was recorded on video using a time-accelerated mode (Video S1), and several snapshots were shown in Fig. 4b. The perovskite stripe area close to the anode side became more and more transparent, and the morphology in this area was completely different from other areas with many pin-holes appearing (Fig. S13), which indicates the drift of ions from the anode side. The loss of perovskite material on the anode side indicated that the drifting ions were $V_{Pb}^{\bullet}$ and/or $V_{MA}^{\bullet}$.

The extensive dynamic poling process study of the device under varied electric field, temperature, and perovskite film morphology supported the mechanism of field driven ion drift for the photovoltaic switching, as shown in Fig. S14. Here, a train of voltage pulses with duration of 0.95 s were applied on the devices and the J_{SC} was recorded after each pulse. An elevated temperature and/or applied electric field (by changing either the applied bias or perovskite film thickness) accelerated the poling process (Fig. S14a-b), while the poling was almost frozen at temperature below 0 °C (Fig. S14c). The extent of photovoltaic switching effect was influenced by morphology, stoichiometry and film quality of perovskite films because of their influence on the defect concentration. For example, the poling became more difficult (Fig. S14d-f) in the device with much larger perovskite grain size which was formed by a solvent-annealing process. This can be explained by the reduced vacancy concentration in the solvent-annealed perovskite films due to less grain boundaries because the solvent-annealing increased the grain size from 300 nm to 600~1,000 nm[28]. The device performance statistics during the dynamic poling process with different measurement condition and film morphology is shown in Fig. S14g. These results confirmed that the switchable photovoltaic behavior of the devices is due to the ion drift.

The best device parameters in the single layer vertical structure devices after poling approached that of optimized multiple-layer devices with both electron and hole transporting

layers. This work points to a new direction of perovskite solar cell design using controlled doping of perovskite for homojunction solar cells, reducing device fabrication complexity. The lateral structure device is particularly interesting because it eliminates the need for transparent electrodes, but its efficiency is still limited by the charge carrier diffusion length in present perovskite materials. Further improvement in crystal quality and surface passivation techniques will help to resolve this issue. The perovskite memristors reported here can be read-out by not only electrical pulse but also optical pulses[18]. This work paved the way for a new approach to doping perovskite using electric pulse so that a doping pattern can be programmed and directly written using scanning probe microscopy for memristor array fabrication, which might open up a new application for perovskite materials for optoelectronic computational devices, as viewing the memristors is increasingly being pursued for computing[29,30].

References

1. Lee, M. M. *et al.* Efficient hybrid solar cells based on meso-superstructured organometal halide perovskites. *Science* **338**, 643-647 (2012).

2. Burschka, J. *et al.* Sequential deposition as a route to high-performance perovskite-sensitized solar cells. *Nature* **499**, 316-319 (2013).

3. Liu, M., Johnston, M. B. & Snaith, H. J. Efficient planar heterojunction perovskite solar cells by vapour deposition. *Nature* **501**, 395-398 (2013).

4. Liu, D. & Kelly, T. L. Perovskite solar cells with a planar heterojunction structure prepared using room-temperature solution processing techniques. *Nature Photon.* **8**, 133-138 (2013).

5. Heo, J. H. *et al.* Efficient inorganic-organic hybrid heterojunction solar cells containing perovskite compound and polymeric hole conductors. *Nature Photon.* **7**, 486-491 (2013).

6. Edri, E. *et al.* Elucidating the charge carrier separation and working mechanism of CH3NH3PbI3−xClx perovskite solar cells. *Nature communications* **5**, 3461 (2014).

7. Kojima, A., Teshima, K., Shirai, Y. & Miyasaka, T. Organometal halide perovskites as visible-light sensitizers for photovoltaic cells. *J. Am. Chem. Soc.* **131**, 6050-6051 (2009).

8. Im, J.-H. *et al.* 6.5% efficient perovskite quantum-dot-sensitized solar cell. *Nanoscale* **3**, 4088-4093 (2011).

9. Kim, H.-S. *et al.* Lead iodide perovskite sensitized all-solid-state submicron thin film mesoscopic solar cell with efficiency exceeding 9%. *Scientific reports* **2**, 591 (2012).

10. Choi, T. *et al.* Switchable ferroelectric diode and photovoltaic effect in BiFeO3. *Science* **324**, 63-66 (2009).

11. Grinberg, I. *et al.* Perovskite oxides for visible-light-absorbing ferroelectric and photovoltaic materials. *Nature* **503**, 509-512 (2013).

12. Xiao, Z. *et al.* Efficient, High Yield Perovskite Photovoltaic Devices Grown by Interdiffusion of Solution-Processed Precursor Stacking Layers. *Energy Environ. Sci.* **7**, 2619-2623 (2014).

13. Chen, Q. *et al.* Planar heterojunction perovskite solar cells via vapor assisted solution process. *J. Am. Chem. Soc.* **136**, 622–625 (2013).

14. Yuan, Y., Xiao, Z., Yang, B. & Huang, J. Arising applications of ferroelectric materials in photovoltaic devices. *J. Mater. Chem. A* **2**, 6027-6041 (2014).

15. Stranks, S. D. *et al.* Electron-hole diffusion lengths exceeding 1 micrometer in an organometal trihalide perovskite absorber. *Science* **342**, 341-344 (2013).

16. Xing, G. *et al.* Long-range balanced electron-and hole-transport lengths in organic-inorganic CH3NH3PbI3. *Science* **342**, 344-347 (2013).

17. Snaith, H. J. *et al.* Anomalous Hysteresis in Perovskite Solar Cells. *J. Phys. Chem. Lett.* **5**, 1511–1515 (2014).

18. Guo, R. *et al.* Non-volatile memory based on the ferroelectric photovoltaic effect. *Nature Commun.* **4**, 1990 (2013).

19. Andersson, P., Robinson, N. D. & Berggren, M. Switchable charge traps in polymer diodes. *Adv. Mater.* **17**, 1798-1803 (2005).

20. Yi, H. *et al.* Mechanism of the switchable photovoltaic effect in ferroelectric BiFeO3. *Adv. Mater*. **23**, 3403-3407 (2011).

21. Frost, J. M. *et al.* Atomistic origins of high-performance in hybrid halide perovskite solar cells. *Nano Lett.* **14**, 2584-2590 (2014).

22. Stoumpos, C. C., Malliakas, C. D. & Kanatzidis, M. G. Semiconducting tin and lead iodide perovskites with organic cations: phase transitions, high mobilities, and near-infrared photoluminescent properties. *Inorganic Chemistry* **52**, 9019-9038 (2013).

23. Mizusaki, J., Arai, K. & Fueki, K. Ion-conduction of the Perovskite-type Halides. *Solid State Ionics* **11**, 203-211 (1983).

24. Yin, W.-J., Shi, T. & Yan, Y. Unusual defect physics in CH3NH3PbI3 perovskite solar cell absorber. *Appl. Phys. Lett.* **104**, 063903 (2014).

25. Kim, J., Lee, S.-H., Lee, J. H. & Hong, K.-H. The Role of Intrinsic Defects in Methylammonium Lead Iodide Perovskite. *J. Phy. Chem. Lett*. **5**, 1312-1317 (2014).

26. Wang, Q. *et al.* Qualifying Composition Dependent p and n Self-doping in $CH_3NH_3PbI_3$ *App. Phy. Lett*. **105**, 163508 (2014).

27. Yang, J. J. *et al.* Memristive switching mechanism for metal/oxide/metal nanodevices. *Nature Nanotechnology* **3**, 429-433 (2008).

28. Xiao, Z. *et al.* Solvent-Annealing of Perovskite Induced Crystal Growth for Photovoltaic Device Efficiency Enhancement. *Adv. Mater 26, 6503-6509* (2014).

29. Yang, J. J., Strukov, D. B. & Stewart, D. R. Memristive devices for computing. *Nature Nanotechnology* **8**, 13-24 (2013).

30. Borghetti, J. *et al.* ‘Memristive’switches enable ‘stateful’logic operations via material implication. *Nature* **464**, 873-876 (2010).

Figure Captions:

Fig. 1. Vertical structure photovoltaic devices and their switching behavior. a, Schematics of the vertical structure device. Dark current **(b)** and photocurrent hysteristics **(c)** of the devices under continuous current sweeping at a rate of 0.14 V/s between -2.5 V and 2.5 V. The arrows in the figure show the scanning direction. **d**, Open circuit voltage of the device recorded after repeated poling by ±2.5 V bias for more than 750 circles. Only the first ten and last ten circles were shown. The red dots refer to the V_{OC} of the device after positive and negative poling.

Fig.2. Lateral structure photovoltaic devices and their switching behavior. a, Schematics of the lateral structure devices. **b**, A Au stripe array under microscope (reflective mode), where the electrode spacing (*d*) shown in the enlarged image (bottom) is 8 μm. The lateral photovoltaic devices connected in series were fabricated by depositing uniform perovskite films (300 nm) on preformed Au stripe electrodes with spacing between 8 and 100 μm. **c**, Photocurrents of the device before and after negative and positive poling for a single cell measured at a sweeping rate of 0.05 V/s under 0.25 sun illumination; The arrows in the figure show the scanning direction. **d**, Photocurrents of the lateral photovoltaic devices connected in series measured at a sweeping rate of ~0.05 V/s for each cell. The poling of the lateral photovoltaic devices were conducted by either poling each cell individually or simply poling the whole area between the first and last electrodes.

Fig. 3. Switchable photovoltaic model and mechanism study. a-b, Schematics of ion drift in perovskite during poling, and the accumulated ions in the perovskite near the electrodes induced *p*- and *n*-doping; **c**, Energy diagram of the *p*-*i*-*n* structure after poling; **d**, Schematic image of the devices with some part of the Au electrodes peeled off. The scanning area is also marked as a dashed rectangle in the image; **e-f,** KPFM potential image of the perovskite/Au areas after

positive and negative poling of the perovskite layers (300 nm). **g-h**, Photoluminescence from the thin perovskite layers close to either a PEDOT:PSS electrode or Au electrode. A thin gold electrode (25 nm) was used as the top electrode so the PL emission from the perovskites close to both electrodes can be measured, and a blue light (405 nm) was used to excite only the 25 nm thick perovskite layer close to the electrodes (estimated by the extinction coefficient) of the 1,015 nm thick device. The PL measurement was conducted in-situ during the poling process to exclude other PL changing factors. The peak at 710 nm in Fig. 3g is from ITO.

Fig. 4. In-situ monitoring of the material change in a poling process. a, Illustration of the setup used for the in-situ monitoring of the poling process using a lateral structure device. **b**, Snapshots of the in-situ recorded video which shows changed perovskite material close to the anode side during the poling process. The electrical field applied on the perovskite film was ~1.2 V/μm.

Methods

CH_3NH_3I precursor synthesis. Methylammonium iodide (CH_3NH_3I) was synthesized using the method described by Michael M. Lee, *et. al* [1]. A concentrated aqueous solution of hydroiodic acid (HI) (15.0 mL, 57 wt% in water, Alfa Aesar) was reacted with methylamine (CH_3NH_2) (13.5 mL, 40 wt% in aqueous solution, Alfa Aesar) at 0 °C for 2 h with constant stirring under nitrogen atmosphere. Methylammonium iodide was crystalized through removing the solvent by a rotary evaporator. The generated white powder was washed with diethyl ether (Alfa Aesar) three times and dried in vacuum overnight.

Film formation and device fabrication. Poly(3,4-ethylenedioxythiophene): poly(4-styrenesulfonate) (PEDOT:PSS) (Baytron-P 4083) was spin-coated on clean indium tin oxide (ITO) substrates at a speed of 3,000 rounds per minute (rpm). The films were then annealed at 105 $^{\circ}$C for 30 min. PbI_2 and MAI were first dissolved in dimethylformamide (DMF) and 2-propanol, respectively. The $MAPbI_3$ films were formed by spin coating PbI_2 (400 mg/ml in DMF) and (45 mg/ml in 2-propanol) sequentially at 6,000 rpm for 35 s respectively, followed by thermal annealing at 100 °C for 2 hours. The $MAPbI_{3-x}Cl_x$ films were formed by spin coating PbI_2 (400 mg/ml in DMF) and $MAI_{0.8}Cl_{0.2}$ (45 mg/ml in 2-propanol) sequentially at 6,000 rpm for 35 s respectively, followed by thermal annealing at 110 °C for 1 hour. The $FAPbI_3$ films were formed by spin coating PbI_2 (400 mg/ml in DMF) and FAI (45 mg/ml in 2-propanol) sequentially at 6,000 rpm for 35 s respectively, followed by thermal annealing at 120 °C for 1 hour. The $MAPbBr_3$ films were formed by spin coating $PbBr_2$ (600 mg/ml in DMF) and MABr (65 mg/ml in 2-propanol) sequentially at 6,000 rpm for 35 s respectively, followed by thermal annealing at 100 °C for 1 hour. After spin coating of the above inorganic materials, the films were dried at 70 °C for 30 min before spin coating the organic part. For the solvent-annealing of

perovksite films, around 10 μL DMF was introduced into the petri-dishs during the thermal-annealing process. The devices were finished by the thermal evaporation of 50 nm gold (Au) as electrode.

For lateral photovoltaic devices, the Au stripe arrays were first fabricated on glass substrates by photolithography, i.e. the 50 nm thick Au layer was thermally deposited on a pre-patterned photoresist layer, and then the photoresist was removed by acetone. The positive photoresistor, Shipley S-1813, was used. The resulted Au stripe patterns have a length of 3 mm, and spacing of 8 μm (Fig. 2b). The total width of the lateral photovoltaic devices connected in series composing of 125 cells is ~1.4 mm. Perovskite films were then fabricated on these substrates with the same method as in vertical device fabrication. The resulted structure of the lateral devices is schematically shown in Fig. 2a. The thickness of the pervoskite films for both vertical and lateral structure device is 300 nm, excepting those specially labeled.

Film and device characterization. The steady-state photocurrent curves were measured under simulated AM 1.5G irradiation (100 mW/cm^2) using a Xenon-lamp-based solar simulator (Oriel 67005, 150 W Solar Simulator). A Schott visible-colour glass-filtered (KG5 colour-filtered) Si diode (Hamamatsu S1133) was used to calibrate the light intensity before photocurrent measurement. A Keithley 4200 semiconductor analyzer was used to apply scanning bias and test the output current simultaneously. All the electrical tests for vertical devices were conducted in glove box. The lateral solar cell measurement was conducted in a probe station chamber which is under vacuum of 10^{-3} Torr, wherein the light (25 mW/cm^2) was incident through a quartz window. A Keithley 240a High Voltage Supply with a maximum voltage output of 1,200 V was used for the poling process. The electrical field applied on the perovskite film is ~1.2 V/μm for 100 s. The poling of the cells was conducted by either poling each cell individually or simply

poling the whole area between first and last electrodes. For the lateral device, the poling bias lasted for ~100 s, which is longer than that in the vertical device due to the much longer ion drift distance. After poling, the *I-V* curves were measured by Keithley 2400.

Observation of the in-situ poling process under microscope The in-situ observation of the ion drift under electric field was carried out by locating the samples under an optical microscope (Olympus BX61), which has a high resolution CCD camera integrated (Photometrics, CoolSNAP-cf). The optical microscope worked at transmission mode with the sample illuminated from bottom side. The samples were kept in a steady N_2 flow during the poling process to prevent the absorption of oxygen and moisture.

Kelvin probe force microscopy (KPFM), atomic force microscopy (AFM) and piezoresponse force microscopy (PFM) measurements. KPFM and AFM measurements were carried out with Dimension Icon, Bruker Inc in air and in the dark. Platinum-iridium coated conductive probes (SCM-PIT, Bruker) were used in the KPFM and AFM measurements. PeakForce KPFM mode combining the Tapping mode AFM with Frequency Modulation-KPFM can measure the topographic and surface potential signal of the same area. The scanning area and tip velocity was 20 μm × 20 μm square and 81.4 μm/s respectively. The lift height for KPFM measurement was 80 nm for all samples. PFM were performed by applying a high-frequency modulating voltage (200–600 kHz, 1.0–1.5 V) to the Pt–Ti-coated silicon (Mikromasch) or Au-coated SiN tips (Olympus). Local piezoelectric hysteresis loops were measured in fixed locations on the film as a function of a dc bias superimposed on ac modulation voltage.

For the sample preparation, the vertical structure devices were first poled in glovebox. Then most areas of the top gold electrodes were peeled off by Scotch tape, but some small areas of the Au electrode were purposely left as the reference for KPFM surface work function.

Ferroelectricity characterization. The ferroelectric polarization measurements were carried out with the Precision Premier II from the Radiant Technologies, Inc at room temperature, and 77 K by soaking the samples into liquid nitrogen for 10 min before the measurements. The applied voltage scanning rate was 0.08 V/s, which is comparable or slower than the rate of photocurrent scanning for switchable photovoltaic effect study. The data was collected by the software package "Vision" integrated in the Precision Premier II.

Acknowledgements

We thank the National Science Foundation for its financial support under Awards ECCS-1201384 and ECCS-1252623, Department of Energy under Award DE-EE0006709 and Defense Threat Reduction Agency under award HDTRA1-14-1-0030.

Author contributions

J. H. conceived and supervised the project. Z. X. fabricated and measured the vertical structure device. Y. Y. and Q. W. fabricated and measured the lateral structure device. Y. S. conducted the KPFM measurement. Q. D. synthesized the MAI material. P.S. and A. G. conducted the PFM measurement. All authors analyzed the data and wrote the manuscript. †Z. X, Y. Y and Y. S contributed to this work equally.

Competing financial interests

The authors declare no competing financial interests.

Figure 1

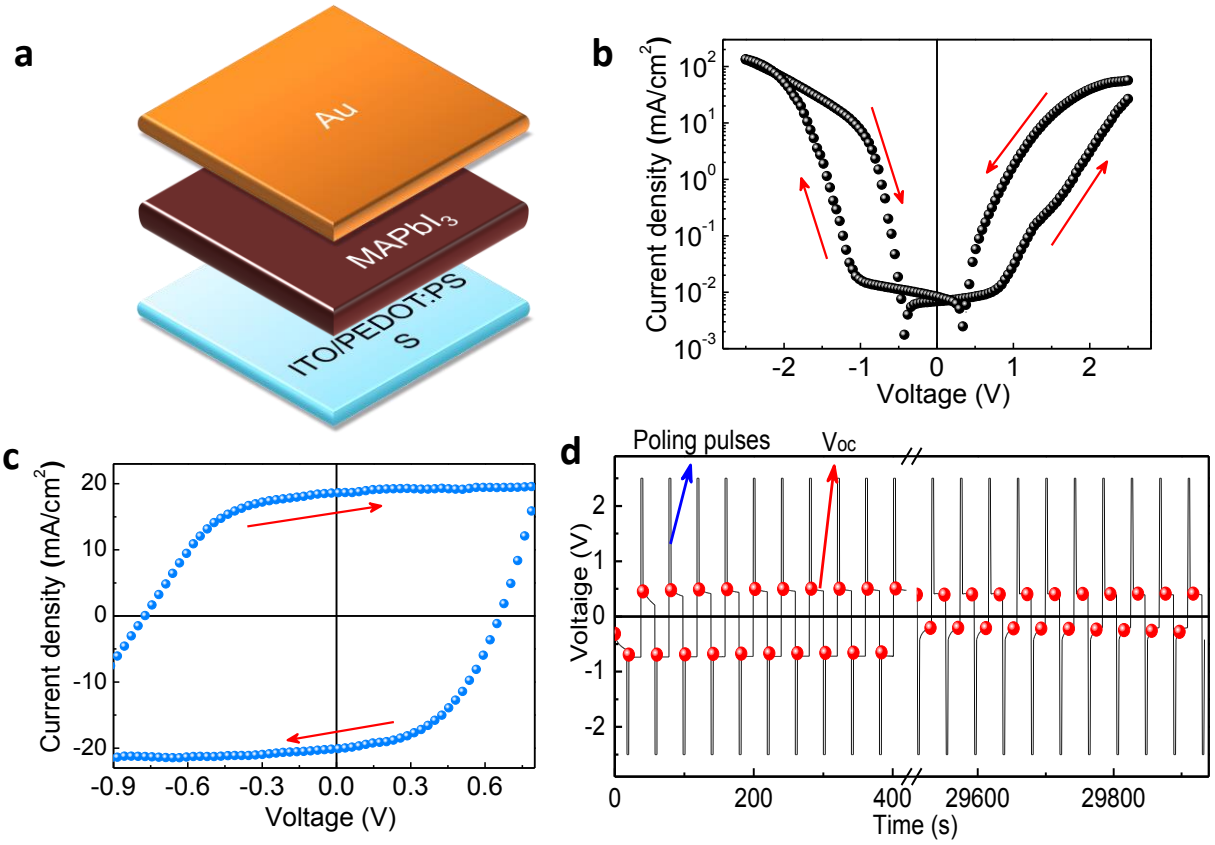
a
Au
MAPbI3
ITO/PEDOT:PSS
b
Current density (mA/cm2)
Voltage (V)
c
Current density (mA/cm2)
Voltage (V)
d
Poling pulses
Voc
Voltaige (V)
Time (s)

Figure 2

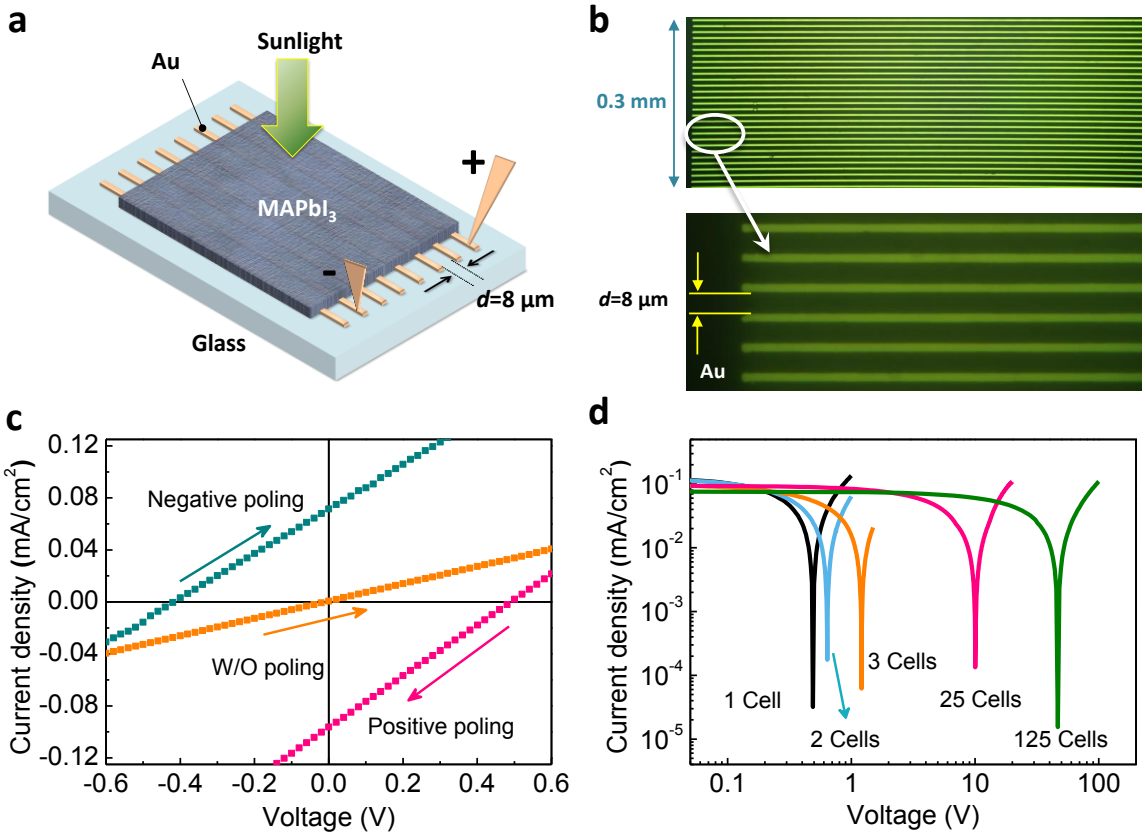
a
Sunlight
Au
MAPbI3
+
-
d=8 µm
Glass
b
0.3 mm
d=8 µm
Au
c
Current density (mA/cm2)
Negative poling
W/O poling
Positive poling
Voltage (V)
d
Current density (mA/cm2)
1 Cell
2 Cells
3 Cells
25 Cells
125 Cells
Voltage (V)

Figure 3

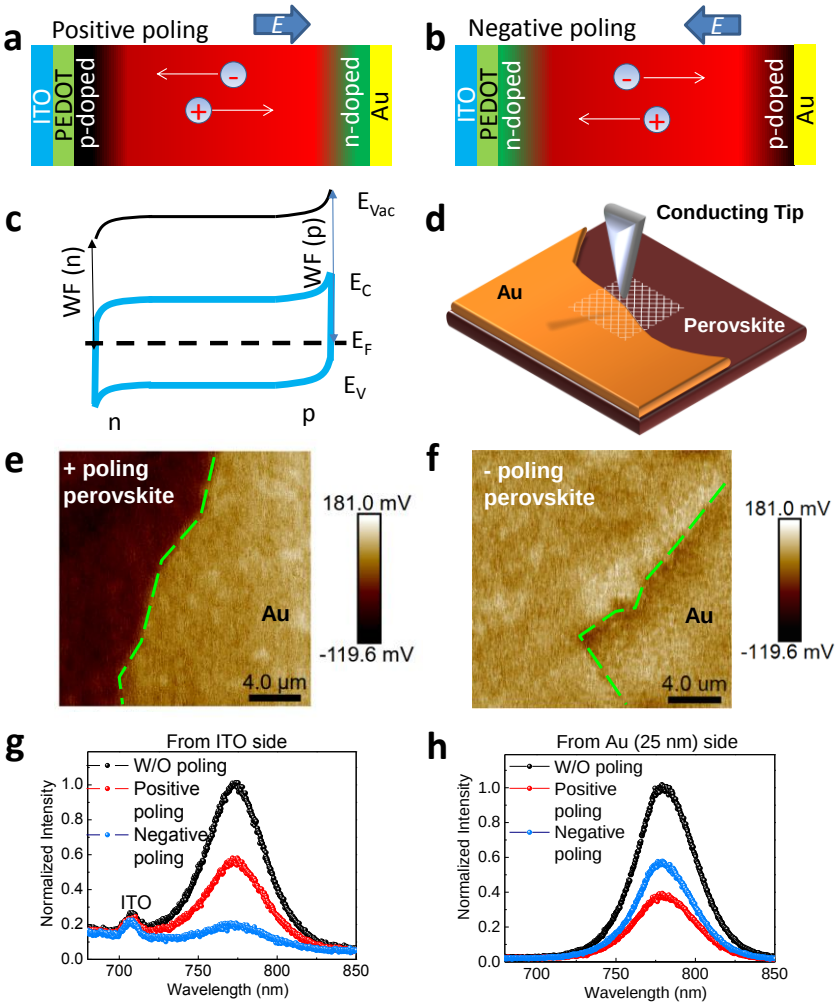
a
Positive poling
E
ITO
PEDOT
p-doped
n-doped
Au
b
Negative poling
E
ITO
PEDOT
n-doped
p-doped
Au
c
WF (n)
WF (p)
E_Vac
E_C
E_F
E_V
n
p
d
Conducting Tip
Au
Perovskite
e
+ poling perovskite
Au
4.0 μm
181.0 mV
-119.6 mV
f
- poling perovskite
Au
4.0 um
181.0 mV
-119.6 mV
g
From ITO side
W/O poling
Positive poling
Negative poling
ITO
Normalized Intensity
Wavelength (nm)
h
From Au (25 nm) side
W/O poling
Positive poling
Negative poling
Normalized Intensity
Wavelength (nm)

Figure 4

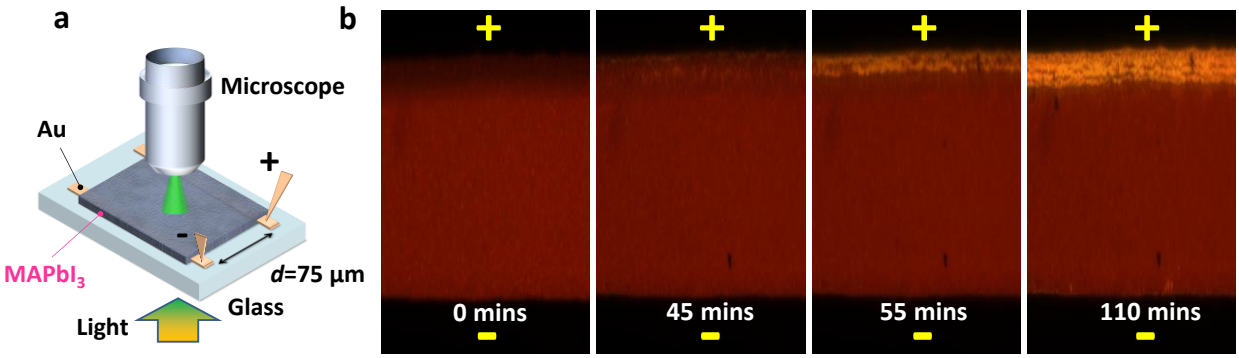
a
b
Microscope
Au
+
-
MAPbI3
d=75 µm
Glass
Light
+
+
+
+
0 mins
45 mins
55 mins
110 mins
-
-
-
-